International Journal of Solids and Structures 47 (2010) 1361–1374

Contents lists available at ScienceDirect

International Journal of Solids and Structures

journal homepage: www.elsevier.com/locate/ijsolstr

Experimental characterization and model identification of directional hardening effects in metals for complex strain path changes

S.H.A. Boers [a,*], P.J.G. Schreurs [a], M.G.D. Geers [a], V. Levkovitch [c], J. Wang [d], B. Svendsen [b]

[a] Mechanics of Materials Section, Dept. of Mechanical Eng., Eindhoven University of Technology, Eindhoven, The Netherlands
[b] Dortmund University of Technology, Institute of Mechanics, Dortmund, Germany
[c] Beck-Arndt Associates, Berlin, Germany
[d] MAN Truck and Bus, Beijing, China

ARTICLE INFO

Article history:
Received 14 November 2008
Received in revised form 23 November 2009
Available online 6 February 2010

Keywords:
Directional hardening modeling
Elastic springback
Sheet forming
Plain strain pure bending

ABSTRACT

The purpose of the current work is the development and application of a new experimental technique and testing device for investigating the complex behavior of sheet metals during non-proportional loading. The method is based on plain strain pure bending, enabling the investigation of large deformation cyclic reversed loading, orthogonal pure bending, as well as springback. The key feature of the pure bending experiment is the absence of contact forces, material slip and friction. Furthermore, during the pure bending test, the strain gradient through the thickness is kinematically prescribed because the specimen is subjected to a plane strain condition in de direction parallel to the rotational axis (Tan et al., 1995), which allows for a straightforward comparison of the pure bending experiments and parallel simulations. The latter is used here via the identification of a recent model for directional hardening effects and arbitrary strain path changes, (Wang et al., 2006, 2008). The current method facilitates experimental investigation of hardening stagnation after reverse loading and cross hardening going well beyond that which is possible with existing methods based on the cyclic shear or tension-shear of sheet metal strips (Bouvier et al., 2005, 2006a,b; Flores et al., 2007.), or pure and three-point bending (Omerspahic et al., 2006; Antonelli et al., 2007; Carbonnière et al., 2009; Yoshida et al., 1998; Weinmann et al., 1988).

1. Introduction

Sheet metal forming operations are generally analyzed using conventional Forming Limit Diagrams (FLD's) which are based on proportional loading experiments. However, even in a single-step forming process like deep-drawing, non-proportional strain path changes are mostly present. It is known that this leads to results which cannot be predicted by classical FLD's.

Many studies (Viatkina, 2005; Bouvier et al., 2003; Haddadi et al., 2006; Nesterova et al., 2001a,b) show that the complex strain path dependency is the result of interaction of the material microstructure evolution and the loading conditions. In other studies (Bouvier et al., 2006a,b, 2005), the effect of loading path changes on the evolution of dislocation structures is investigated and it is shown that the resulting hardening effects cannot be described by standard isotropic and kinematic hardening models.

Several material models try to capture the additional hardening effects by decomposing the stress evolution in two parts: one for the response to proportional loading and the other for non-proportional effects, such as the additional hardening (Zhao and Kuang, 2006).

Other models, based on that of Teodosiu and Hu (1998a, 1997), have been used by a number of authors (e.g., Li et al. (2003b,a), Bouvier et al. (2006a,b, 2003, 2005), Hiwatashi et al. (1997, 1998)) to model the additional anisotropic hardening effects for non-proportional strain paths. These models all originate from the original Teodosiu model, and account for directional hardening effects due to a reorientation of persistent planar dislocation structures upon changes in loading direction. The directional hardening behavior is also influenced by the effective polarity of excess dislocation pile-ups at these structures. In addition, the Teodosiu model deals with standard kinematic and isotropic hardening effects. The influence of persistent planar dislocations is represented by an internal variable: a stress-like fourth-order symmetric tensor decomposed into dynamic and latent parts, characterizing the interaction between the previously formed persistent dislocation structure and the current inelastic flow direction. Others use a micromechanical approach in order to account for non-proportional strain path dependent effects (Viatkina, 2005; Peeters et al., 2001b,a, 2002).

Recent work Wang et al. (2006, 2008) has shown that, in contrast to experimental results for many steels like DC06, the

* Corresponding author. Tel.: +31 40 247 4022.
E-mail address: s.h.a.boers@tue.nl (S.H.A. Boers).

0020-7683/$ - see front matter © 2010 Elsevier Ltd. All rights reserved.
doi:10.1016/j.ijsolstr.2010.01.022

Teodosiu model (Teodosiu and Hu, 1998a, 1997) does not predict directional or cross hardening (i.e., a transitory increase of the yield stress after an orthogonal change of loading path direction) during continuous loading path changes. As shown in Wang et al. (2006, 2008), the problem here lies in the modeling of the fourth-order directional hardening tensor. They developed an alternative model for this tensor which correctly accounts in particular for the effect of latent directional hardening during continuous loading path changes. Their model is used in the current work.

So far, most of the experiments used to determine the material parameters for the Teodosiu model are done with a combination of uniaxial tensile tests and shear tests which enable both orthogonal and Bauschinger strain path changes. The effect of directional hardening on e.g., the elastic springback behavior has been investigated for several materials, however, additional boundary effects such as stress concentration and material slip at the clamps can be a classical source of inaccuracies. This paper presents a newly developed mechanical test in which a pure bending moment can be applied to a sample, eliminating the influence of friction, contact forces and slip. Like simple shear tests, Lou et al. (2007), Wang et al. (2008), the pure bending experiment also allows for large strains in cyclic loading. A rectangular sample is clamped and either the bending angle or the bending moment can be controlled. An accurate and straightforward procedure can be carried out to compare the numerical results to the experimental results.

In Section 2, the key features of the material model and the effects of arbitrary strain path changes on the hardening behavior will be recalled. Section 3 introduces several experimental tools, among which the pure bending experiment, that are used to investigate reversed loading tests and orthogonal strain path changes. Section 4 presents the strategy and fitting procedure in order to determine the model parameters for DC06 steel. Section 5 will present an independent set of experiments and numerical results for the verification and Section 6 finally concludes the chapter.

2. Material model

This section reviews the phenomenological representation of evolving hardening behavior in terms of changes in the size, center and shape of the yield surface offers the means to characterize the behavior of many metals of interest during complex, non-proportional loading processes present in many technological processes (e.g., cup deep-drawing). The challenge here lies in the connection of such changes in the yield surface geometry with the underlying microscopic and physical mechanisms of grain and dislocation microstructural development in polycrystalline metals. One basic expectation in this regard is that the grain microstructure in sheet metals is determined almost solely by the rolling process. Forming processes like cup drawing are expected to result in little or no change in this microstructure. Consequently, during forming processes, yield surface evolution is generally expected to be due almost solely to an evolving dislocation microstructure at the grain- or grain-cluster level. Persistent dislocation structures resulting for example in cross hardening are thought to form primarily during monotonic deformation, i.e., in a given loading direction. Plastic slip taking place on slip planes parallel to this direction is observed (e.g., Nesterova et al., Nesterova et al. (2001a,b)) to result in the development of wall-like dislocation structures separating dislocation cells of different crystallographic orientation. These walls are thought to consist of both dipolar and polar dislocations (e.g., Peeters et al. (2001b,a, 2002)), the latter arising in order to accommodate the misorientation arising between adjacent dislocation cell-blocks across the wall.

In the context of complex non-proportional loading histories involving reverse (tension-compression) or orthogonal (e.g., tension-shear) paths such as those shown in Fig. 1, the evolution of such dislocation microstructures have a pronounced effect on the material behavior.

For example, as shown in case 3 in Fig. 1, reverse shear loading preceeded by sufficiently-large shear preloading results in significant hardening followed by stagnation and then resumed hardening. The extent of strain hardening stagnation increases with the amount of preshear. This phenomenon has first been observed in Hasegawa and Yakou (1975), Christodoulou et al. (1986) and occurs both in f.c.c. and b.c.c. polycrystals whenever the amount of prestrain is sufficiently large. The cross hardening effect has been observed in DC06 automotive steel and will be the subject of investigation in this paper.

An orthogonal change of loading path direction, for example from tension to shear, results in the activation of new, previously inactive glide systems in the new loading direction. Being orthogonal to the new loading direction, the planar dislocation microstructures formed during the first loading stage are thought to act as an additional barrier to the activation of dislocation motion in the new loading direction. This results in an increase of the effective yield stress above the monotonic level upon orthogonal change of loading direction. After activation, dislocations glide in the new direction resulting in a break-down of the old dislocation microstructure and a corresponding reduction of the yield stress level back down to the monotonic level.

All of these effects are captured in the current material model, which has been presented in detail in Wang et al. (Wang et al., 2008). This model is embedded in the framework of the standard multiplicative decomposition $\boldsymbol{F} = \boldsymbol{F}_{\mathrm{E}} \cdot \boldsymbol{F}_{\mathrm{P}}$ of the deformation gradient $\boldsymbol{F}$ into elastic $\boldsymbol{F}_{\mathrm{E}}$ and plastic $\boldsymbol{F}_{\mathrm{P}}$ parts Simo and Hughes (1998). As obtained elsewhere (Wang et al., 2008), this decomposition together with the right polar decomposition $\boldsymbol{F}_{\mathrm{E}} = \boldsymbol{R}_{\mathrm{E}} \cdot \boldsymbol{U}_{\mathrm{E}}$ of $\boldsymbol{F}_{\mathrm{E}}$ and the assumption of small elastic strain yields the system

$$\begin{aligned} \overset{\nabla}{\ln \boldsymbol{U}}_{\mathrm{E}} &= \boldsymbol{R}_{\mathrm{E}}^{\mathrm{T}} \cdot \boldsymbol{D} \cdot \boldsymbol{R}_{\mathrm{E}} - \boldsymbol{D}_{\mathrm{P}}, \\ \dot{\boldsymbol{R}}_{\mathrm{E}} &= \boldsymbol{W} \cdot \boldsymbol{R}_{\mathrm{E}} - \boldsymbol{R}_{\mathrm{E}} \cdot \boldsymbol{W}_{\mathrm{P}}, \end{aligned} \tag{1}$$

of evolution relations for $\ln \boldsymbol{U}_{\mathrm{E}}$ and $\boldsymbol{R}_{\mathrm{E}}$, respectively, derived in an incremental context. Here, $\boldsymbol{D} = \mathrm{sym}(\boldsymbol{L})$ is the continuum rate of deformation, $\boldsymbol{D}_{\mathrm{P}} = \mathrm{sym}(\boldsymbol{L}_{\mathrm{P}})$ its inelastic counterpart, $\boldsymbol{W} = \mathrm{skw}(\boldsymbol{L})$ the continuum spin, and $\boldsymbol{W}_{\mathrm{P}} = \mathrm{skw}(\boldsymbol{L}_{\mathrm{P}})$ the plastic spin. Restricting the current formulation to the case of sheet metal forming, it is reasonable to assume that the texture in these materials achieved during rolling remains largely unchanged during forming processes like tension, compression, simple shear, cyclic simple shear, and combinations of these. In this case, $\boldsymbol{W}_{\mathrm{P}}$ is negligible, and the evolution of $\boldsymbol{R}_{\mathrm{E}}$ depends only on $\boldsymbol{W}$, in which case it reduces to a purely kinematic quantity (i.e., the Jaumann rotation). In addition, focusing in this work on the material behavior of sheet metal during forming below the forming limit, we assume here for simplicity that damage or any other process resulting in inelastic volume changes are neglible. In this case, plastic incompressibility $\det(\boldsymbol{F}_{\mathrm{P}}) = 1$ pertains, implying $\mathrm{tr}(\boldsymbol{D}_{\mathrm{P}}) = 0$ and $\boldsymbol{D}'_{\mathrm{P}} = \boldsymbol{D}_{\mathrm{P}}$ in the incremental context.

Since the elastic range and elastic strains are small, any texture effects from rolling leading to an anisotropic elastic behavior are assumed to have a negligible impact on the material behavior. In this case, the isotropic form

$$\boldsymbol{M} = \kappa\, \mathrm{tr}(\boldsymbol{E}_{\mathrm{E}})\boldsymbol{I} + 2\mu \boldsymbol{E}'_{\mathrm{E}} \tag{2}$$

is assumed for the Mandel stress $\boldsymbol{M}$ in terms of the elastic strain $\boldsymbol{E}_{\mathrm{E}} = \ln \boldsymbol{U}_{\mathrm{E}}$, bulk modulus κ (where $\kappa = \lambda + \frac{2}{3}\mu$), shear modulus μ, and deviatoric part $\boldsymbol{E}'_{\mathrm{E}}$ of $\boldsymbol{E}_{\mathrm{E}}$. Lastly, again in the framework of small elastic strain, $\boldsymbol{M}$ and $\boldsymbol{R}_{\mathrm{E}}$ determine the Kirchhoff stress $\boldsymbol{K}$ via

$$\boldsymbol{K} = \boldsymbol{R}_{\mathrm{E}} \cdot \boldsymbol{M} \cdot \boldsymbol{R}_{\mathrm{E}}^{\mathrm{T}}. \tag{3}$$

Consequently, in contrast to $\boldsymbol{K}' = \boldsymbol{R}_E \cdot \boldsymbol{M}' \cdot \boldsymbol{R}_E^T$, $\mathrm{tr}(\boldsymbol{K}) = \mathrm{tr}(\boldsymbol{M})$ of $\boldsymbol{K}$ is independent of $\boldsymbol{R}_E$.

The current model for anisotropic yield behavior due to dislocation microstructure development Wang et al. (2006, 2008) is closely related to that of Teodosiu and Hu (1998a,b). Since the two models predict qualitatively different behavior in the case of continuous loading path changes, however, they are clearly distinct. Central to these models is the Teodosiu form

$$\phi = \sqrt{\boldsymbol{\Sigma} : {}^4\boldsymbol{A} : \boldsymbol{\Sigma}} - r - f\,|{}^4\boldsymbol{S}| \tag{4}$$

of the yield function. Here, $\boldsymbol{\Sigma} = \boldsymbol{M} - \boldsymbol{X}$ is the effective stress, $\boldsymbol{X}$ the back stress, and r is the yield stress. Further, ${}^4\boldsymbol{A}$ is the Hill initial flow orthotropy tensor, and ${}^4\boldsymbol{S}$ a traceless, symmetric fourth-order tensor-valued internal variable whose evolution accounts for the dependence of the current effective yield stress on the history of the directional strength of oriented (e.g., laminate-like cell-wall) dislocation structures. This is weighted by the material constant f determining the fraction of the dislocation walls strength contributing to isotropic hardening. In the context of (4), the model hardening behavior is determined in particular by the Voce form

$$\dot{r} = c_r\,(r_{sat} - r)\,\dot{\alpha}_P \tag{5}$$

for the evolution of r in terms of the corresponding saturation rate c_r and saturation value r_{sat} for r. Here, α_P is the accumulated equivalent inelastic deformation. The initial value of r is given by the initial yield stress σ_{Y0}. In the current rate-independent context, α_P is determined as usual by the consistency condition. Analogous to the isotropic case, kinematic hardening is modeled here via the Armstrong–Frederick form

$$\dot{\boldsymbol{X}} = c_x\,(x_{sat}\boldsymbol{N}_P - \boldsymbol{X})\,\dot{\alpha}_P \tag{6}$$

for the evolution of the back stress $\boldsymbol{X}$. This evolution is then governed by the saturation rate c_x and saturation magnitude x_{sat} of $\boldsymbol{X}$, as well as by the direction $\boldsymbol{N}_P = \boldsymbol{D}_P/|\boldsymbol{D}_P|$ of the rate of inelastic deformation

$$\boldsymbol{D}_P = \dot{\alpha}_P\,\partial_{\boldsymbol{\Sigma}}\phi \tag{7}$$

given here in associated form. The initial value of $\boldsymbol{X}$ is assumed to be zero. x_{sat} is not constant, but rather varies with ${}^4\boldsymbol{S}$ (see below). The evolution relation for ${}^4\boldsymbol{S}$ is based on the idea that currently active and previously active (i.e., latent) glide systems both contribute to the growth, saturation and break-down of oriented dislocation structures related to cross hardening. On this basis, the evolution of ${}^4\boldsymbol{S}$ is given by

$${}^4\dot{\boldsymbol{S}} = c_d\,\{h_p\,s_{sat}\,{}^4\boldsymbol{N}_P - (h_p + h_x)\,{}^4\boldsymbol{S}_d\}\,\dot{\alpha}_P - c_l\,(|{}^4\boldsymbol{S}_l|/s_{sat})^{n_l}\,{}^4\boldsymbol{S}_l\,\dot{\alpha}_P. \tag{8}$$

Here, ${}^4\boldsymbol{S}_d = ({}^4\boldsymbol{N}_P : {}^4\boldsymbol{S}) : {}^4\boldsymbol{N}_P$ is the projection of ${}^4\boldsymbol{S}$ parallel to ${}^4\boldsymbol{N}_P = \boldsymbol{N}_P \otimes \boldsymbol{N}_P$ and represents the strength of dislocation structures associated with the currently active slip systems. Likewise, ${}^4\boldsymbol{S}_l = {}^4\boldsymbol{S} - {}^4\boldsymbol{S}_d$ is the projection of ${}^4\boldsymbol{S}$ orthogonal to ${}^4\boldsymbol{N}_P$ and represents the strength of the dislocation structures associated with the latent slip systems. Material constants appearing in (8) include the saturation rates c_d and c_l, the saturation magnitude s_{sat}, and the exponent n_l. In particular, the latter determines the influence of

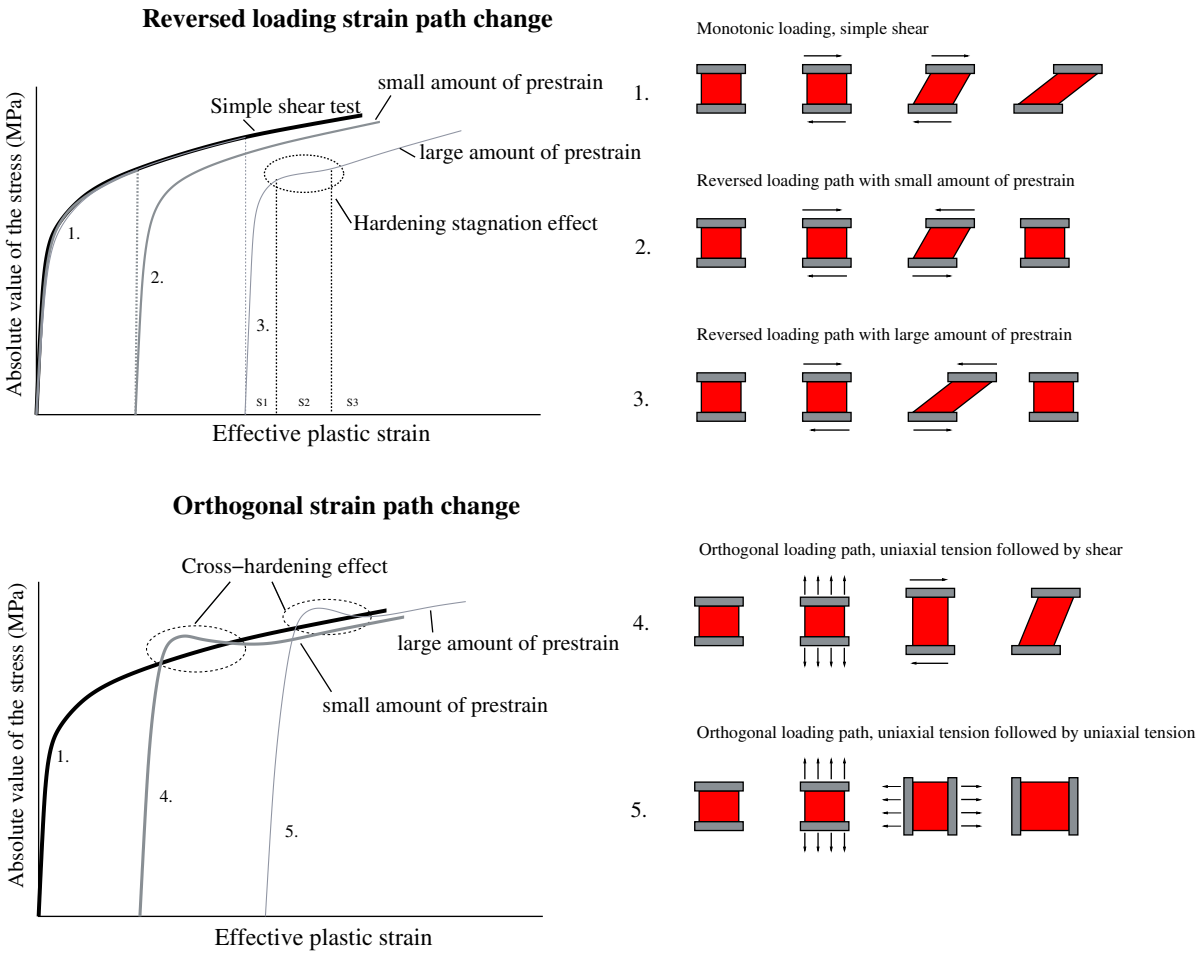

Fig. 1. The effect of different loading paths on the macroscopic material response for monotonic, reversed and orthogonal strain paths.

Table 1
Model parameter values for AKQD steel, according to Teodosiu and Hu (1997).

Parameter	Value
c_p	2.7
c_x	50.0
c_d	2.7
c_l	2.7
c_r	0.0
f	0.59
m	2.4
n_l	3.0
n_p	0.2
Stress parameters	
λ	121.2 GPa
μ	80.8 GPa
σ_{Y0}	51.0 MPa
x_0	64.0 MPa
r_{sat}	0.0 MPa
s_{sat}	145.0 MPa
Hill parameters	
F	0.5
G	0.5
H	0.5
L	1.5
M	1.5
N	1.5

prestraining on the evolution of ${}^4\boldsymbol{S}_l$. The material function h_p governs the contribution to the evolution of ${}^4\boldsymbol{S}_d$ arising from dislocation polarization processes. The magnitude of these contributions depends in particular on the projection $\boldsymbol{N}_P : \boldsymbol{P}$ which accounts for the effect of the net polarity of excess dislocations building up at dislocation sheets on the hardening behavior. Its evolution is described through

$$\dot{\boldsymbol{P}} = c_p (\boldsymbol{N}_P - \boldsymbol{P}) \dot{\alpha}_P, \tag{9}$$

with c_p the corresponding saturation rate. Together with $\boldsymbol{N}_P$ and ${}^4\boldsymbol{S}, \boldsymbol{P}$ determines the form of the function h_p appearing in (8), which also depends on a further material exponent n_p. This function determines the influence of $\boldsymbol{P}$ on the development of ${}^4\boldsymbol{S}$. Likewise, the influence of determining the influence of $\boldsymbol{X}$ on the development of ${}^4\boldsymbol{S}$ is given by the function h_x depending on $\boldsymbol{X}$ and $\boldsymbol{N}_P$. The effect of variable h_x will be more explained in Section 2.1. Lastly, the saturation magnitude x_{sat} of $\boldsymbol{X}$ is given by the constitutive relation

$$x_{sat} = x_0 + (1 - f)\sqrt{|{}^4\boldsymbol{S}_d|^2 + m|{}^4\boldsymbol{S}_l|^2} \tag{10}$$

depending on the directional strength of the dislocation microstructure. Here, x_0 represents the initial value of x_{sat}. The parameter m determines the influence of latent as opposed to current dislocation structures on the saturation magnitude x_{sat} of $\boldsymbol{X}$. For more details, the reader is referred to Wang et al. (2006, 2008). The above relations contain a total of 21 material parameters. These include the two elastic constants κ and μ, the initial yield stress σ_{Y0}, the six Hill anisotropy parameters F, G, H, L, M, N determining ${}^4\boldsymbol{A}$, the saturation rate parameters c_r, c_x, c_d, c_l, and c_p, as well as the remaining hardening parameters $m, x_0, f, r_{sat}, s_{sat}, n_l$, and n_p. This completes the model formulation.

2.1. Numerical results

In this section some numerical results demonstrating the behavior of the current material model are presented. The parameters that have been used were initially determined for aluminum-killed mild steel (AKDQ) with a 0.036% carbon content and an average grain size of 50 μm, by Teodosiu and Hu (1998b,a). The parameters are listed in Table 1.

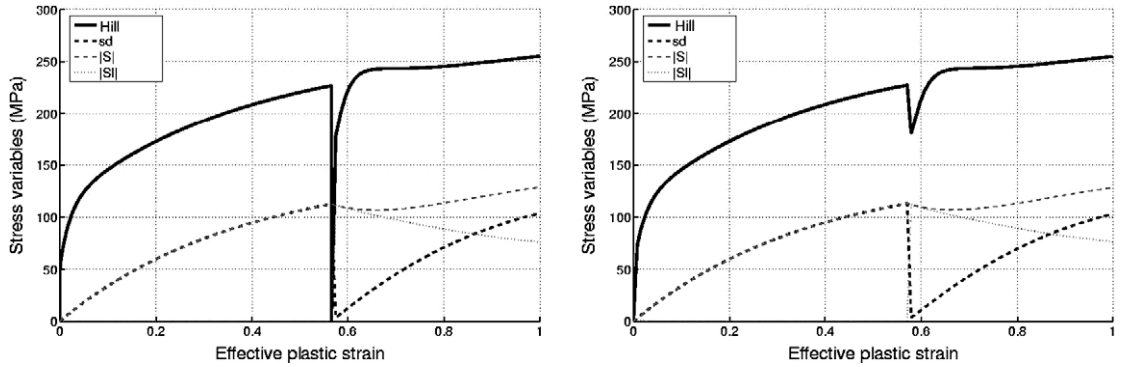

Fig. 2. The evolution of the Hill equivalent stress and the distortional hardening variables. The left and right figure show the results for an orthogonal strain path change with and without unloading, respectively.

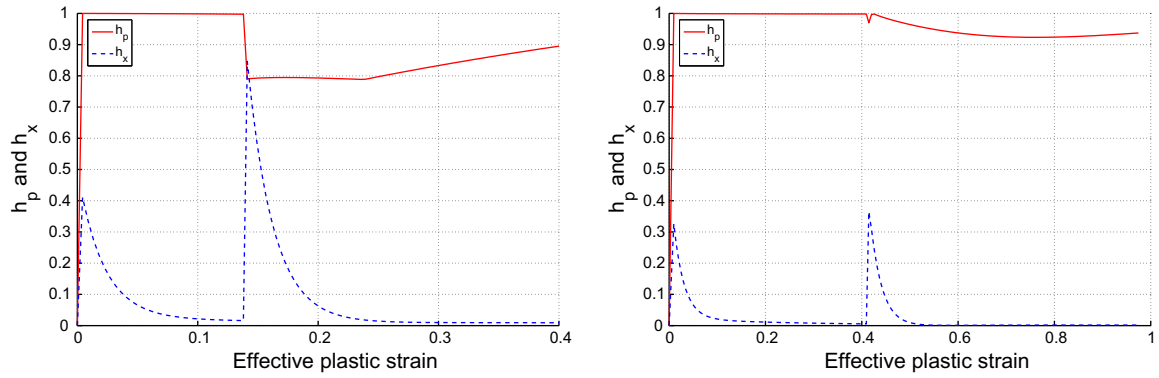

Fig. 3. The evolution of the internal parameters h_p and h_x. The figures show the results for a reversed simple shear test (a) and a simulation where a uniaxial tensile test is followed by a simple shear test (b).

Table 2
Chemical composition of the DC06 steel.

Element	C	Mn	P	S	Ti
wt%	0.02	0.25	0.020	0.020	0.3

In Fig. 2a and b, two orthogonal strain path changes are simulated, one with elastic unloading and the second one without.

As can be seen for both cases, the latent parts $\|^4\boldsymbol{S}_l\|$ evolve exactly the same. For the original formulation of the Teodosiu model, the latent part would remain zero after the strain path change without elastic unloading.

In Fig. 3, the evolution of h_p and h_x are presented for a reversed shear test (a) and a test (b), where uniaxial tension is followed by simple shear. It can be seen that the evolution of h_x is only very limited in the case (b) and even in the reversed loading test, the value for h_x only takes some significant values immediately after the change in loading direction. The decrease of h_p immediately after the strain path change during the reversed loading test reflects the work-hardening stagnation effect, see Fig. 1.

3. Experimental characterization

This section presents several experimental tools which are used in Section 4 for determining a complete set of parameters of the material model for DC06 automotive steel, manufactured at Corus RD&T in the Netherlands. The 0.7 mm thick cold rolled interstitial free (IF) steel complies with the European standard EN 10130:1999 and is known for its excellent forming and deep-drawing capacities. During all experiments, the rolling direction of the material must be well defined with respect to the experimental setup. The chemical composition of the DC06 material is given in Table 2.

3.1. Uniaxial tension and simple shear

Teodosiu and co-workers based the main features of their model on the material response during uniaxial tension and simple shear. These two experiments are sufficient to investigate monotonic loading and both experiments enable a reversed and orthogonal strain path change. All their material parameters were determined by these two experiments.

Besides classical tensile devices, enabling uniaxial and plane-strain tensile tests, a pure bending device is here used to apply a pure bending moment on a test specimen. The advantage of this test is that large amplitude cyclic loading can be performed up to strains of 60%, which is not possible in ordinary tensile tests in combination with simple shear tests. Furthermore, the strain distribution through the specimens is non-homogeneous, in contrast to the simple shear and uniaxial tests. Considering these differences and actual deformations in forming processes, the complementarity of this test is obvious. For clarity, Fig. 4 presents the definition of the axes of the sample with respect to the loading directions of the uniaxial tensile test, the simple shear test and

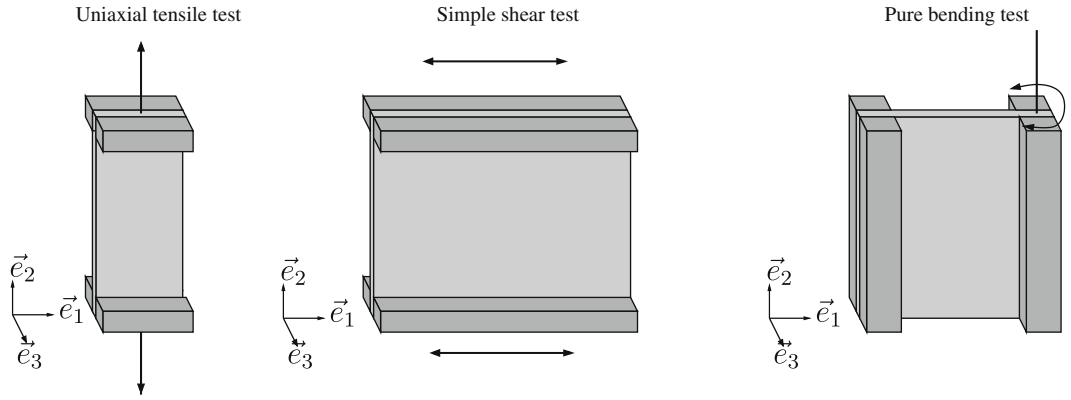

Fig. 4. The principal directions are presented for the uniaxial tensile test, the simple shear test and the pure bending experiment.

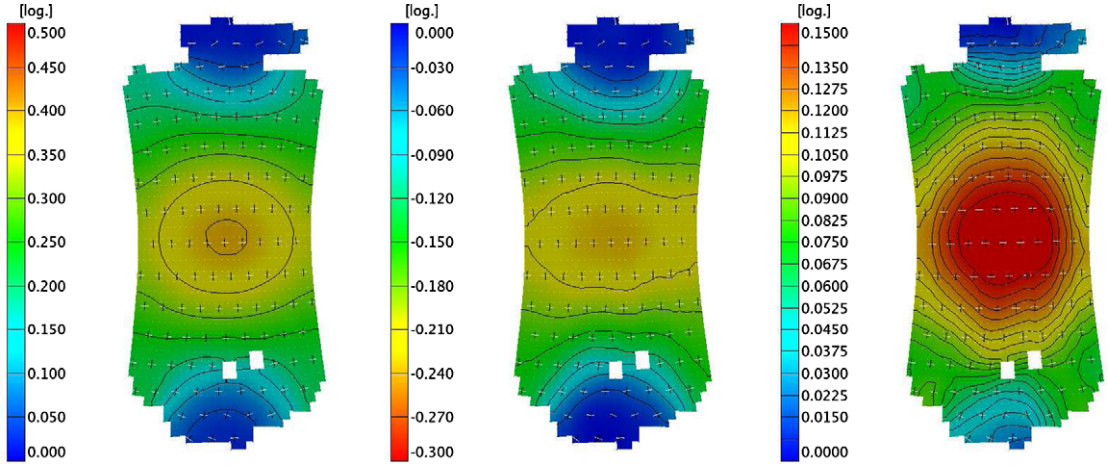

Fig. 5. The result for a sample, DC06 steel, that was strained up to 50% during an uniaxial tensile test, in a–c, the distribution of major strain, minor strain and thickness, is presented, respectively.

the pure bending experiment. In Fig. 4, the sample dimensions in the $\vec{e}_1, \vec{e}_2$ and $\vec{e}_3$ directions are $20 \times 40 \times 0.7$ mm^3 during a uniaxial tensile test.

3.2. Strain measurement

For determining strains, a photogrammetry method is used. In Fig. 5, the results are presented for a rectangular specimen ($60 \times 100 \times 0.7$ mm^3) subjected to uniaxial loading up to 50% in the tensile direction. The rolling direction is parallel to the $\vec{e}_2$-direction as well. Before straining takes place, a regular grid is etched onto the metal surface and afterwards the deformation of the grid is used to determine the in-plane strain components. The thickness reduction is calculated by using the in-plane strain components, since for (large) plastic strains volume invariance can be assumed. In Fig. 5a–c, the results are presented for the major strain, minor strain and the thickness distribution, respectively. Later on in this section, bending specimens will be prepared from larger predeformed tensile specimens. This method is then used to determine the area in which a homogeneous strain distribution can be assumed.

3.3. Plain strain pure bending

Reversed loading, orthogonal strain path changes and elastic springback effects can be well investigated by applying a pure bending moment on a rectangular plate. The sample dimensions imply a plain strain condition in the direction parallel to the rotational axis. A reversed loading test can be trivially performed by simply applying an opposite bending moment (Boers et al., 2009).

During the pure bending experiment, the sides of a rectangular sample (5) are firmly clamped by a pair of hydraulically actuated clamps (3 and 4), see Fig. 6. The clamps are individually mounted on two air-suspended linear guides (1 and 2) that can move frictionless along and around the axes of two cylinders (8 and 9). Because the linear guides are positioned at a relative angle of 90 degrees, no lateral force can be transferred from one clamp to the other. This means that whenever a sample is positioned in the device, the axial and rotational clamp positions are completely determined by the edges of the sample.

During bending, the virtual rotation point of the device during the experiment is determined by the sample as well.

One of the clamps (4) provides the rotation, as indicated in Fig. 6, with an accuracy of 0.01 degrees, whereas the other clamp measures the applied bending moment by using an elastic joint (6) in combination with a set of strain gauges. The bending moment can be measured with an accuracy of 0.02 Nm. The whole setup is positioned on a solid frame (7) and measures approximately $1 \times 1 \times 0.5$ m^3.

The device can be operated in two different modes. In the first mode, the rotation and rotation speed is controlled and in the second mode, the bending moment is controlled. The second mode is generally used to investigate elastic springback effects.

In Fig. 7, the procedure is illustrated in which a reversed and an orthogonal strain path change is explained, in which the different possible processing steps are marked. As a starting point, a rectangular flat sample (1) is clamped in the device (2) and a positive angle is applied through steps 3–6. The maximum positive angle is 180 degrees. Next, the rotation is reversed (7) and e.g. in step 8, the bending moment is zero. The angle difference between step 7 and 8 is exactly the elastic springback after the 180 degrees positive rotation. At this point the sample can be taken out of the device (20) e.g. to investigate the microscopic structure by Orientation Image Microscopy (OIM) but the sample can also be bend to its neutral position (12) and even further to a maximum negative angle of −90 degrees. When e.g. the negative angle in step 13 is sufficient to finish in step 15 with a bending moment equal to zero and an angle of zero degrees, a complete cycle has been carried out and the flat sample can be taken out (16), however, it has a certain deformation history. Then, either reversed loading (Bauschinger test) can be applied by repeating the previous cycle or orthogonal loading can be applied. For the latter choice, the sample sides have to be removed from the center part (18) because these side parts did not plastically deform during the first cycle. Then the sample is rotated by 90 degrees and clamped in the device again. These steps can be varied in order to apply a well defined deformation history to the material. It must be noted that the material in between the clamps undergoes a uniform deformation in the plane of the sheet ($\vec{e}_1$- and $\vec{e}_2$-direction), whereas the strain distribution through the material thickness ($\vec{e}_3$) is non-uniform.

In the next section, the procedure for determining the material parameters for DC06 for the Teodosiu model will be given. The photogrammetry method is used to determine strains during the experiments that are used for prestraining and experiments that are used for determining the anisotropic Hill parameters.

4. Parameter estimation

In this section, the procedure to determine all relevant material parameters for the Teodosiu model for the DC06 steel is explained. Except for the elastic parameters (E-Modulus and Poisson's ratio) which are adopted from the manufacturer and literature. In total, there are 19 material parameters which have to be determined

Pure bending device

1. left linear guide
2. right linear guide
3. left hydraulic clamp
4. right hydraulic clamp
5. sample
6. elastic joint
7. base
8. left cylinder
9. right cylinder

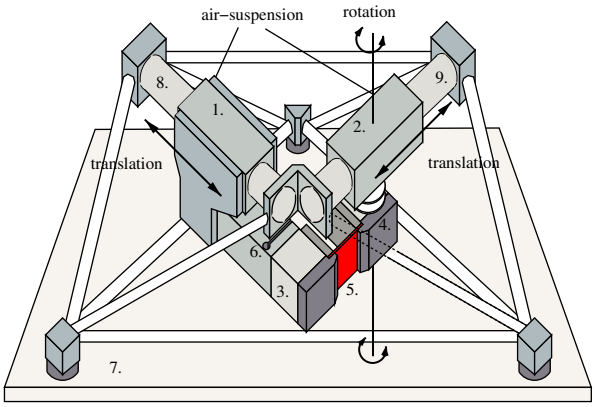

Fig. 6. Pure bending device with air-suspended clamps. The left clamp records the bending moment whereas the right clamp provides the rotation of the sample.

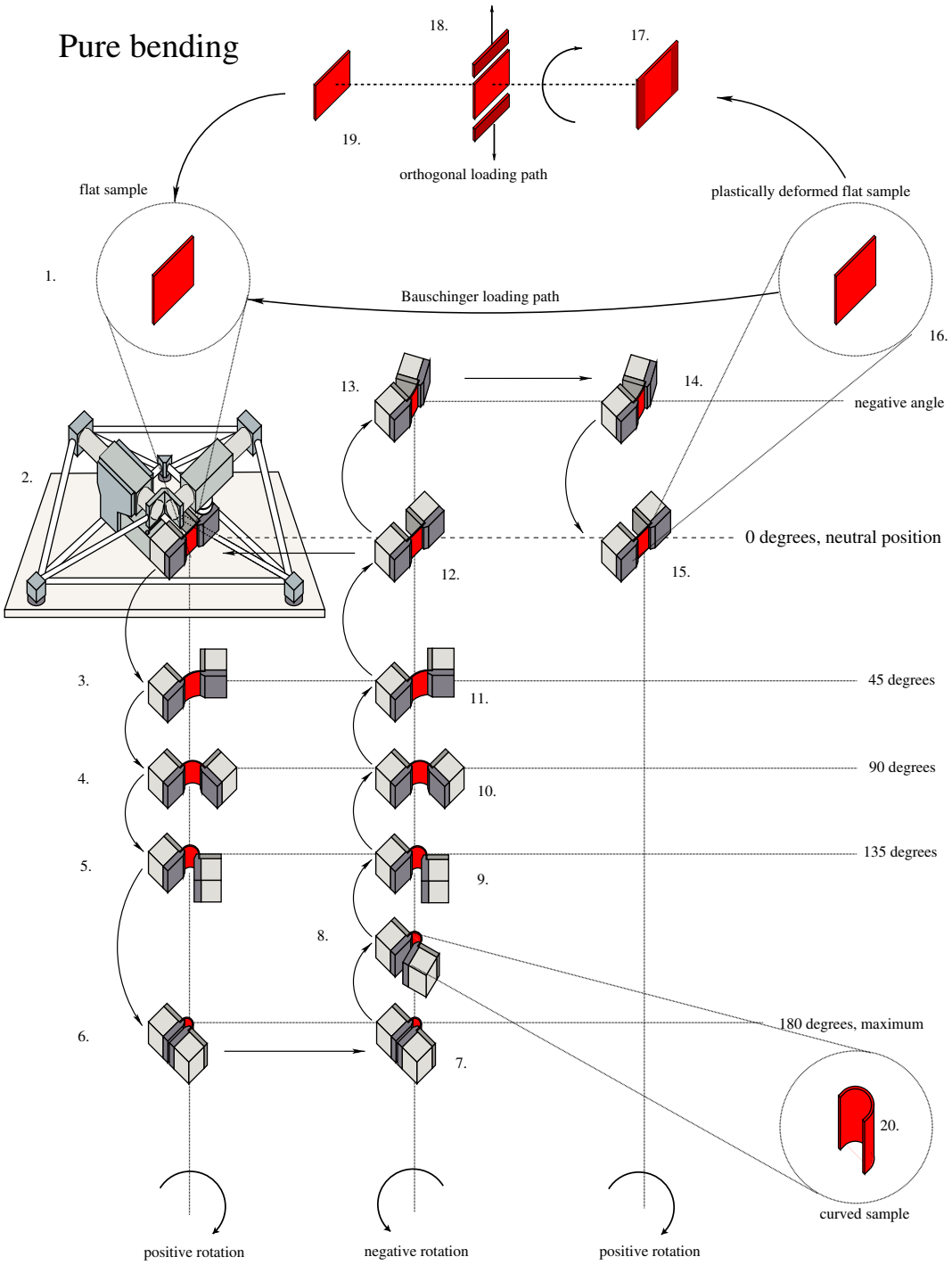

Fig. 7. Schematic representation of the pure bending experiment, allowing for a reversed loading test and an orthogonal strain path test. Possible subsequent forming steps are indicated.

through adequate experimental testing. For each experiment, a separate numerical simulation is done. For the fitting procedure, a finite difference method is used which calculates a sensitivity matrix. Except for the elastic constants and the parameters for the initial yield criterion, all material constants are perturbed, one after the other. The response of the model is calculated for every simulation. The sensitivity matrix is calculated from the differences between the response for the initial (estimated) parameter set and the response of the perturbed set.

First, the two elastic constants will be determined as well as the five parameters determining the initial yield criterion. Next, a set of nine parameters are fitted which primarily determine the material response during monotonic and reversed loading. Finally, an orthogonal pure bending experiment is done to obtain the final three parameters.

4.1. Elastic constants and initial yield stress

The elastic behavior of the material is assumed to be isotropic, and the elastic constants λ and μ are determined by Young's modulus and Poisson's ratio. According to the material specifications, Young's modulus equals 190 GPa and Poisson's ratio equals 0.3.

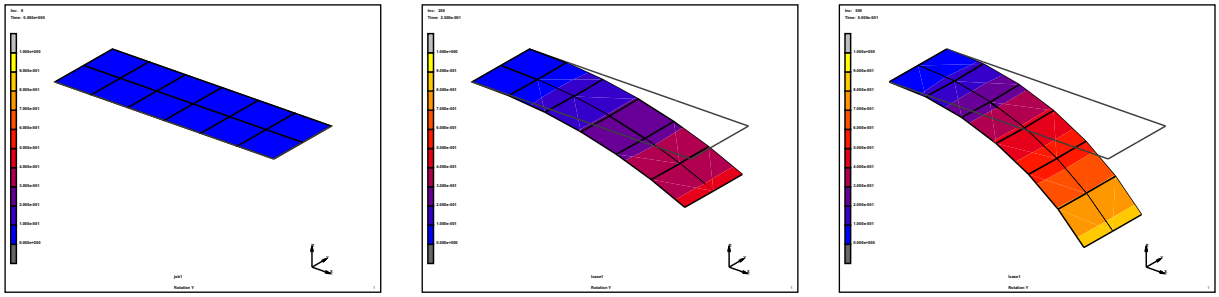

Fig. 8. Simulation of the pure bending experiment in three stages. The element mesh represents only a small segment of the sample since the strain distribution in the plane of the sheet is homogeneous. A rotation along the $\vec{e}_2$-direction is prescribed. The color contours represent the rotation angle around the y-axis.

For λ and μ, this yields a value of 109.6 GPa and 73.1 GPa, respectively. The initial yield stress σ_{Y0} is determined to be 120 MPa.

The anisotropy of initial yielding, reflecting the initial texture, will be described by the Hill'48 yield criterion:

$$\sigma_H^2 = F(s_{22}-s_{33})^2 + G(s_{33}-s_{11})^2 + H(s_{11}-s_{22})^2 + 2Ls_{23}^2 + 2Ms_{31}^2 + 2Ns_{12}^2 \tag{11}$$

where σ_H is the equivalent Hill stress

$$\sigma_H = \sqrt{(\boldsymbol{M}-\boldsymbol{X}) : {}^4\boldsymbol{A} : (\boldsymbol{M}-\boldsymbol{X})} \tag{12}$$

with ${}^4\boldsymbol{A}$ is the fourth-order symmetric traceless orthotropic Hill flow anisotropy tensor and s_{ij} are the components of the effective stress tensor $\boldsymbol{M}-\boldsymbol{X}$ in the axes of orthotropy (Section 2.)

Next, the angle α is defined as the angle between the rolling direction and the $\vec{e}_2$-direction during a uniaxial tensile test. In this analysis, also the change in shape of the yield locus is investigated. The yield locus is determined for different samples which all have a different amount of prestrain. By using the photogrammetry technique, the longitudinal (ϵ_{22}^p) and lateral (ϵ_{11}^p) logarithmic plastic strains are obtained during the experiment, starting from an ϵ_{22}^p of 0.05.

Then, the Lankford coefficient of anisotropy R_L, which is a function of the reduction coefficient q, is determined for various α:

$$R_L(\alpha) = \frac{q}{1-q}; q = -\frac{\epsilon_{11^p}}{\epsilon_{22^p}} \tag{13}$$

The R_L values have been determined experimentally for different amounts of plastic strain, resulting in a set of average R_L values: $R_L(0) = 1.88, R_L(45) = 2.04$ and $R_L(90) = 2.43$. Up to a level of 27% plastic strain in two directions, the experimentally observed variations in the R_L values is less than 9% with respect to the average R_L values. These observations are in good correspondence with the specified minimal R_L value for this DC06 steel of 1.8 determined by Corus RD&T. The introduction of the average R_L values enables coupling the Lankford coefficient R_L to α:

$$R_L(\alpha) = \frac{4H-(F+G+4H-2N)\sin^2(2\alpha)}{2((G-F)\cos(2\alpha)+F+G)} \tag{14}$$

$G+H=1$ is given by the condition: the yield locus should fit the yield stress for a uniaxial tensile test along the rolling direction. Consequently, the set of parameters for initial anisotropy is reduced to 3 independent parameters: F, G and N. Solving the equations yields F = 0.269, G = 0.347, H = 0.653 and N = 1.56.

At this point, already seven material parameters have been determined: λ, μ, σ_{Y0}, and the anisotropic Hill parameters F, G, H and N. In the next sections, the focus will be on the evolution of the plastic material behavior and the corresponding parameters.

4.2. Monotonic and reversed cyclic loading

In this section, four experiments are carried out where the scalar $\beta = \boldsymbol{A}_1 : \boldsymbol{A}_2$ varies between 1 or −1, where $\boldsymbol{A}_1$ and $\boldsymbol{A}_2$ represent the direction of the strain rate tensor before and after the strain path change, respectively. By means of a parameter fitting procedure, nine parameters are determined:

- r_{sat}, the saturation value for the isotropic hardening r representing the randomly oriented dislocation structures, as a function of the effective plastic strain.
- c_r, controlling the evolution rate of isotropic hardening.
- s_{sat}, the saturation value for the isotropic hardening term $\|{}^4\boldsymbol{S}\|$ representing the dislocation structures, as a function of the effective plastic strain.
- c_d, controlling the evolution rate of the dynamic part of $\|{}^4\boldsymbol{S}\|$.
- n_p, controlling the evolution rate of the hardening term s_d. When n_p is increased, the recovery of the hardening term s_d after reversed loading is slowed down.
- c_p, controlling the saturation rate of $\boldsymbol{P}$.
- f, the fraction of the hardening caused by oriented dislocation structures. When f equals 0, the directional hardening due to oriented dislocation structures is fully assigned to the kinematic hardening term $\boldsymbol{X}$.
- x_0, being the initial value of the saturation value for the backstress.
- c_x, controlling the saturation rate of the backstress as a function of the effective plastic strain.

4.2.1. Pure bending

The first experiment, is the pure bending experiment, which can be considered as a series of simultaneous plane-strain tensile and compression test through the thickness. The effective thickness reduction is zero. The presence of both compression and tension stresses at any time enable repeated reversed bending tests without necking. The sample dimensions are $10 \times 100 \times 0.7$ mm^3. The sample is bend in five cycles, each cycle to 125 degrees and back to 0 degrees.

The pure bending simulations are performed with four-noded quadrilateral shell elements with 19 layers through the thickness, where layer 1 represents the surface layer. Each node has six degrees of freedom and the bending angle is prescribed on the edge of the element mesh. Theoretically, the simulation can be performed with only one element since the strain distribution in the plane of the sample is uniform, however for clarity a more elaborate element mesh is used (Fig. 8) representing a segment of the sample in the test specimen.

4.2.2. Plane-strain tension

A plane-strain tensile test is performed (courtesy of Maarten van Riel, UTwente) without strain in the $\vec{e}_1$-direction. The sample dimensions are $45 \times 3 \times 0.7$ mm^3. During this test, the lateral strain ϵ_{11} can be neglected and the only strain components are the ϵ_{33} and the ϵ_{22} components. The ϵ_{22} strain is monitored by means of strain gauges and is used to determine the true stress.

4.2.3. Uniaxial tension

A uniaxial tensile test is carried out on a sample with dimensions of $60 \times 120 \times 0.7$ mm^3. Strains are measured with the photogrammetry method up to 45% of plastic strain in the $\vec{e}_2$-direction at 10 intermediate stages in order to determine the in-plane strain components. Combining the reaction force and the strain measurements, provides the true stress during the experiment at 10 stages until the onset of necking.

4.2.4. Simple shear

A simple shear test has been performed (courtesy of Maarten van Riel, UTwente) which completes the set of experiments in this section, see Fig. 4.

The nine indicated parameters are next fitted for the four experiments. The two elastic parameters from the previous section are used and the remaining three other parameters have no significant influence on the numerical response for now, except for the simple shear simulation where a small evolution of the latent part ${}^4\boldsymbol{S}_l$ is observed. As a consequence, these three parameters have to be determined/fitted with another set of experiments, as will be described further on. The procedure yields the following set of parameter values: $r_{sat} = 82$ MPa, $c_r = 17, s_{sat} = 128$ MPa, $c_d = 11, n_p = 28, c_p = 5.87$, $f = 0.26, x_0 = 17.95$ MPa, $c_x = 151$.

In Fig. 9, on the left, the experimental results are presented for the plane-strain tensile test, the uniaxial tensile test and the simple shear test, as well as the numerical predictions with the Teodosiu model and the set of fitted parameters. On the right, the results are presented for the pure bending experiment.

It was found that c_r, which controls the saturation speed of the isotropic hardening, has a big effect on the material hardening in the beginning of the uniaxial, plane-strain and simple shear test up to 0.2 true/shear strain, whereas a considerable effect in the pure bending experiment is seen during the first cycle (0–125–0 degrees). The saturation value r_{sat}, s_{sat} and the combination of f and c_x determine the level of the reaction moment after cycle 2 as well as the hardening behavior during the monotonic tests after 0.2 true/shear strain.

This is in accordance with the results presented in Figs. 10 and 11, where it can be seen that the evolution of $\|{}^4\boldsymbol{S}\|$ stagnates after an effective plastic strain of 0.4, and so does $|\boldsymbol{X}|$ and r. In the bending experiment this is represented by a stagnation of the reaction bending moment after two cycles. It is believed that the difference between the monotonic tests and the numerical predictions, after 0.3 of true/shear strain, is due to the evolution of texture, which is not incorporated here. The loading path change from bending to unbending in the FE-structural context is not abrupt, but rather takes place continuously and inelastically. In this case, the corresponding change from tension $(\beta = 1)$ to compression $(\beta = -1)$ is also continuous and therefore goes through zero. As such, ${}^4\boldsymbol{S}_l$ becomes activated and will develop as shown in Fig. 10. However,

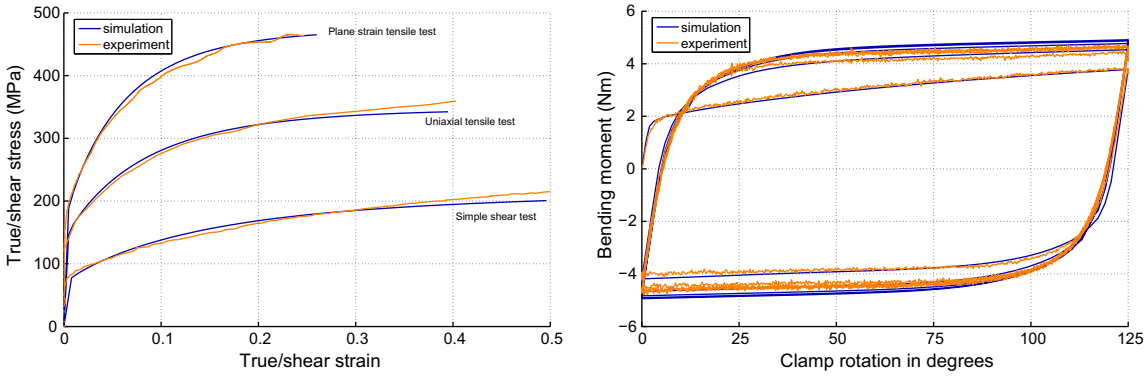

Fig. 9. On the left, the plane-strain tensile test, the uniaxial tensile test and the simple shear test. On the right, the result from the pure bending experiment where a sample is bend over 5 cycles, each from 0 to 125 degrees and back.

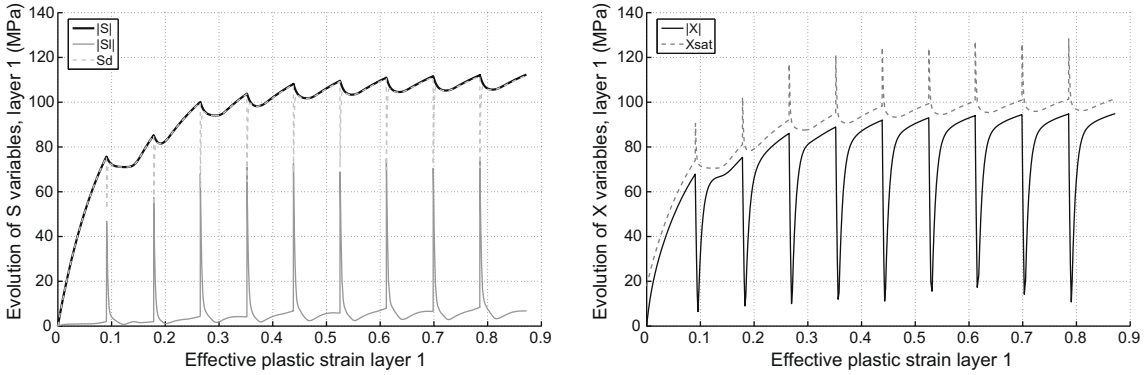

Fig. 10. Numerical results for the bending simulation. For layer 1, on the left, the evolution of the ${}^4\boldsymbol{S}$ variables, on the right, the evolution of the backstress variables, all as a function of the effective plastic strain.

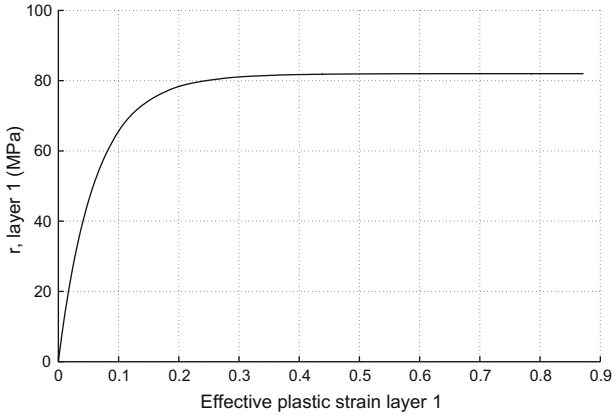

Fig. 11. The numerical results for the bending experiment. The evolution of the isotropic hardening variable r as a function of the effective plastic strain, for layer 1.

the effect is very small and as such has a negligible influence on the hardening behavior as a whole.

In Fig. 12, the behavior of the h_p and h_x parameters are presented for the pure bending experiment. It is clear that the value for h_p drops to zero immediately after the loading direction is reversed. Its evolution is determined by the set of parameters: c_d, c_p, s_{sat} and n_p. The value for h_x has only a non-negligible value after the abrupt change in loading direction, and plays only a minor role.

4.3. Orthogonal loading experiments

The parameters that are determined in this section are:

- c_l, for the latent part of the evolution Eq. (8).
- n_l, the exponent in Eq. (8) governing the evolution of ${}^4\boldsymbol{S}_l$ due to prestraining.
- m, for the extra contribution of the latent part ${}^4\boldsymbol{S}_l$ for determining x_{sat} through Eq. (10).

For these parameters, an evolution of ${}^4\boldsymbol{S}_l$ must be realized and therefore orthogonal experiments are carried out. One experiment, which already has been introduced, is the simple shear test. An additional orthogonal experiment is performed in which the material is first prestrained during the pure bending experiment. A rectangular sample with dimensions of $20 \times 100 \times 0.7$ mm^3 is bend three times to an angle of 135 degrees and back to zero degrees. Then, a negative angle of 7 degrees is applied in order to obtain a perfectly flat sample that can be taken out of the device. From this prestrained specimen, two samples are prepared of which one is used for a reversed pure bending test, and the other for an orthogonal pure bending test. The effective sample dimensions are $20 \times 20 \times 0.7$ mm^3.

With the fitting procedure, the values $c_l = 1.95, n_l = 0, m = 2.5$ are obtained. In Fig. 13 on the left, the result of the pre-deformation is presented along with the corresponding numerical prediction. On the right, the reaction moments of the reversed and orthogonal bending experiments are presented together with the numerical predictions. The complete set of fitted parameters is used and an adequate agreement between numerical and experimental results is revealed.

Although the transitory hardening effects during the bending tests are less pronounced compared to tensile-shear deformation tests, the bending moment for the orthogonal bending experiment is considerably higher compared to the reversed loading experiment. The reason why the transitory hardening effect is less pronounced is essentially related to the non-uniform distribution of

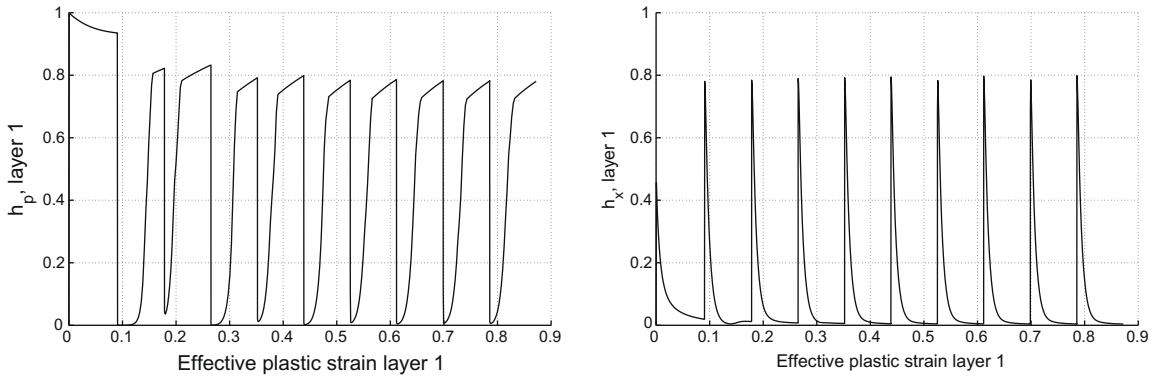

Fig. 12. On the left, the evolution h_p, and on the right the evolution of h_x, as a function of the effective plastic strain.

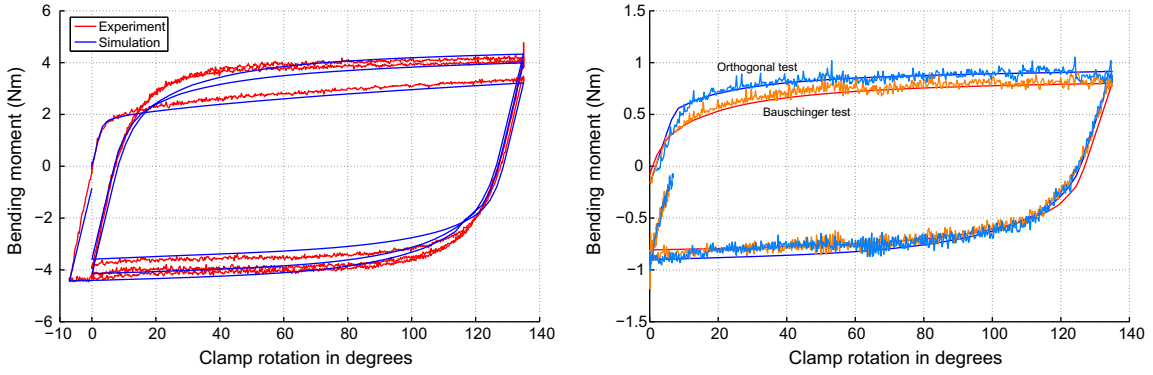

Fig. 13. The left figure shows the reaction moment as a function of the rotation. During the pre-deformation the specimen is bend three times to 135 degrees.

the stresses through the specimen thickness. The next set of figures indicate the evolution of the distortional hardening variables. After three cycles, the effective plastic strain in layer 1 is approximately 0.26. For the orthogonal bending experiment, Fig. 14 on the left, an abrupt change is observed for the evolution of $\|^4\boldsymbol{S}_I\|$. After the strain path change, the corresponding value for $\|^4\boldsymbol{S}\|$ however, is not significantly higher compared to the reversed bending experiment after 0.26 effective plastic strain.

The higher level of the bending moment during the orthogonal test mainly results from the evolution of the backstress components, immediately after the strain path change, see Fig. 15. After 0.26 effective plastic strain, x_{sat} and as a consequence, $|\boldsymbol{X}|$ increase considerably. The value for f of 0.26 also effectively contributes to an increase of hardening through the backstress components.

The increase of the backstress just after the strain path change is caused by the instantaneous increase of the h_p parameter as can be seen in Fig. 16 on the left, leading to a strong increase of the backstress after the orthogonal strain path change and an increase in the bending moment compared to the reversed loading experiment.

4.4. Parameters

To conclude this chapter, all parameters are presented in Table 3.

It can be concluded that the values for s_{sat} and c_d are substantially different compared to the values as determined by Bouvier

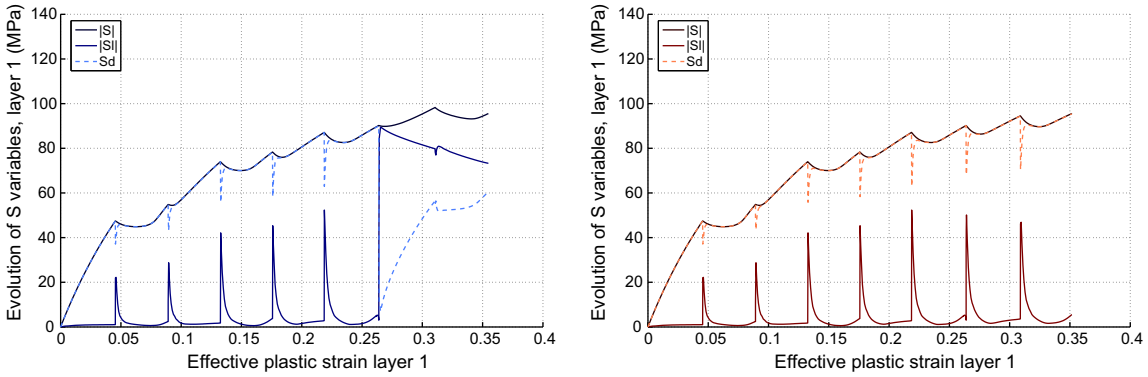

Fig. 14. The evolution of the $\|^4\boldsymbol{S}\|$ variables for the orthogonal and the reversed bending test, respectively.

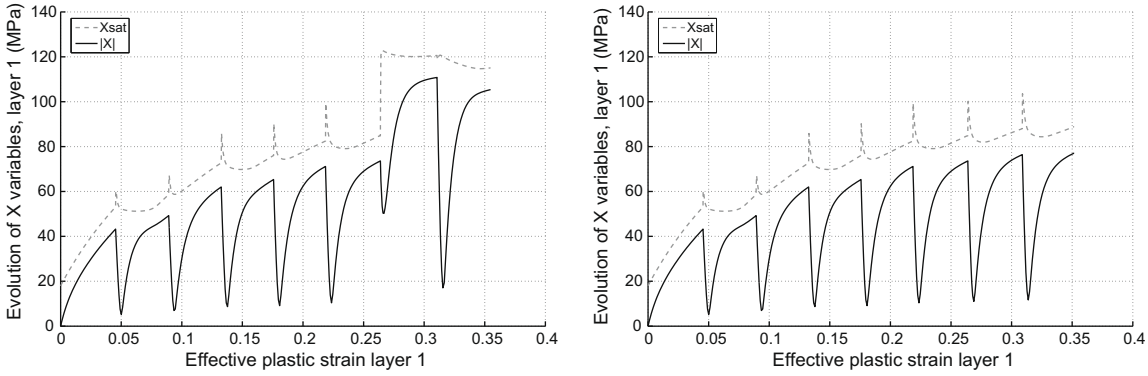

Fig. 15. The evolution of the backstress variables for the orthogonal and the reversed loading test, respectively.

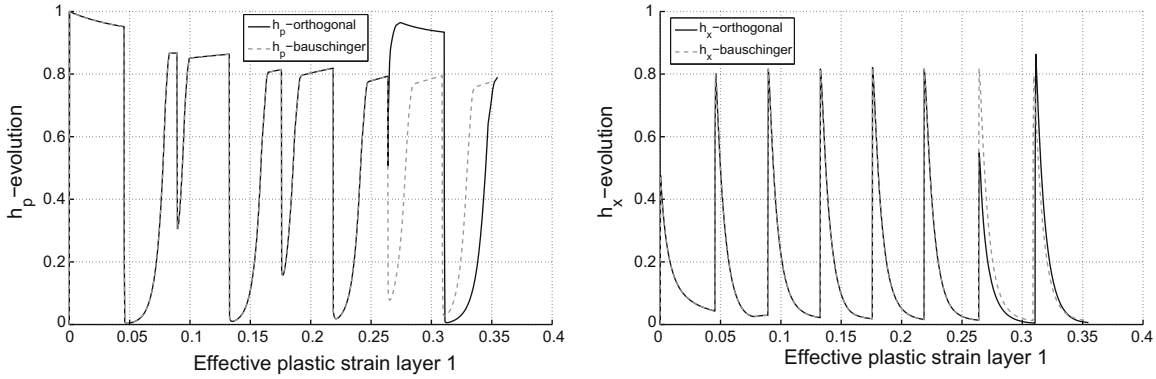

Fig. 16. The evolution of h_p and h_x for the orthogonal and the reversed loading bending test, respectively.

Table 3
Parameters of the Teodosiu model for DC06 steel, obtained from samples with a thickness of 0.7 mm produced at Corus.

Parameter	Value
c_p	5.87
c_x	151.0
c_d	11.0
c_l	1.95
c_r	17.0
f	0.26
m	2.5
n_l	0.0
n_p	28.0
Stress parameters	
λ	109.6 GPa
μ	73.1 GPa
σ_{Y0}	120.0 MPa
x_0	17.95 MPa
r_{sat}	82.0 MPa
s_{sat}	128.0 MPa
Hill parameters	
F	0.269
G	0.347
H	0.653
L	1.5
M	1.5
N	1.56

et al. (2005). In this study the value for s_{sat} and c_d are determined to be 128 MPa and 11, compared to 231 MPa and 4, respectively.

Probably, the material from Bouvier et al. (2005), being produced by a different supplier apparently presents some inherently different material properties, even though both steels are DC06 cold rolled steels according to the European standard EN 10130:1999. However, it is believed that the difference of these fitted parameters can also arise from the experimental data used, which is more extensive here.

One of the key features here is that we investigated the DC06 material response by means of a pure bending experiment, at large amplitude, repeated loading, enabling reversed and orthogonal strain path changes after several cycles of loading and reversed loading. In order to illustrate the difference in the set of parameters, and to rule out the non-uniqueness of the fitted parameter set, the material parameters for the DC06 material by Bouvier et al. (2005) has been used to predict the evolution of the directional hardening variables for the pure bending experiment where the specimen is bend five times to 125 degrees and back to zero. The results are presented in Fig. 17.

From Fig. 17 on the left, it is clear that the evolution of $\|^4\boldsymbol{S}\|$ is very similar up to an effective plastic strain of 0.25. This corresponds to the first two cycles during the pure bending experiment. The increase of $\|^4\boldsymbol{S}\|$ beyond that point results in an increase of the saturation value for the backstress and would cause the material to harden considerably more, resulting in an overestimated value for the reaction bending moments for cycles 3–5. It is believed that the pure bending experiment clearly enhances the accuracy of the determination of the model parameters with respect to the saturation value s_{sat}.

5. Verification and evaluation

This section presents the results of a set of independent experiments and numerical predictions by using the set of material parameters determined in the previous section.

5.1. Tensile-bending experiments

First, two independent pure bending tests are done on the as-received material, where the rolling direction is either the $\vec{e}_2$ or the $\vec{e}_1$ direction. No significant difference in the reaction moments can be noticed. Next, a series of experiments are carried out where the material is first deformed during a uniaxial tensile test with the rolling direction parallel to the $\vec{e}_2$-direction. Four different levels of pre-deformation are investigated: 4.4%, 12.5%, 22.9% and 32.5% of strain in the $\vec{e}_2$-direction. These experiments are repeated twice, and from each set two samples are prepared from the center part. By using the photogrammetry method, an area is extracted in which the strain distribution is nearly homogeneous. During the uniaxial tensile tests, the material is strained in the $\vec{e}_2$-direction which results in a thickness reduction and a lateral reduction in the $\vec{e}_1$-direction. Hence, no pure reversed loading or orthogonal loading experiment can be done. After the uniaxial tensile tests, two pure bending experiments are done for each set. During the first bending experiment, the bending axis coincides with the $\vec{e}_2$ tensile direction of the specimen during uniaxial tension. This test will be referred to further on as the reversed bending test. For the other bending test, the bending axis is perpendicular to the tensile direction, which will be referred to as the orthogonal bending test.

Fig. 18 shows the bending moment for the four levels of pre-deformation. For all four pre-deformation strains, the bending moments for the orthogonal bending tests are higher than for the reversed bending tests. The difference increases with the amount of pre-deformation.

5.2. Predictions at large strains

In Fig. 19, three pole-figures are presented for the as-received material and after straining in a uniaxial tensile test up to 10% and 35% in the $\vec{e}_2$ direction, respectively. It is observed that the texture of the material clearly changes due to the amount of

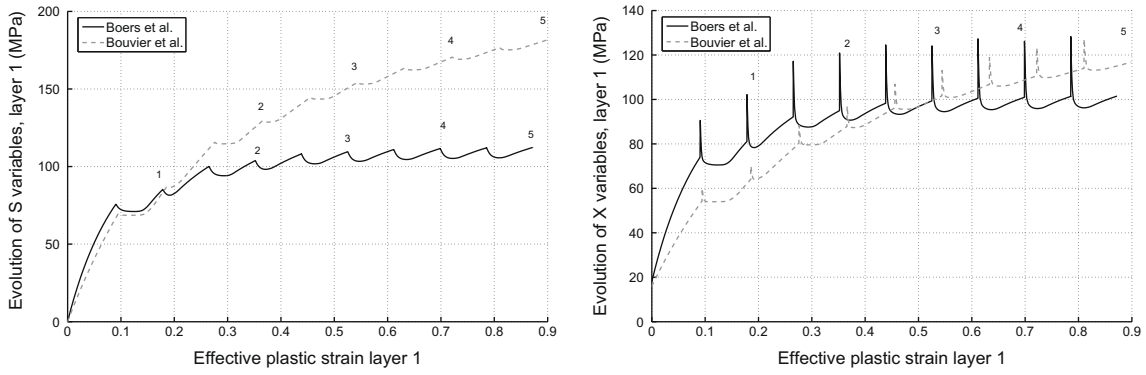

Fig. 17. The evolution of $\|^4\boldsymbol{S}\|$ and the backstress on the left and right, respectively, for different parameter sets.

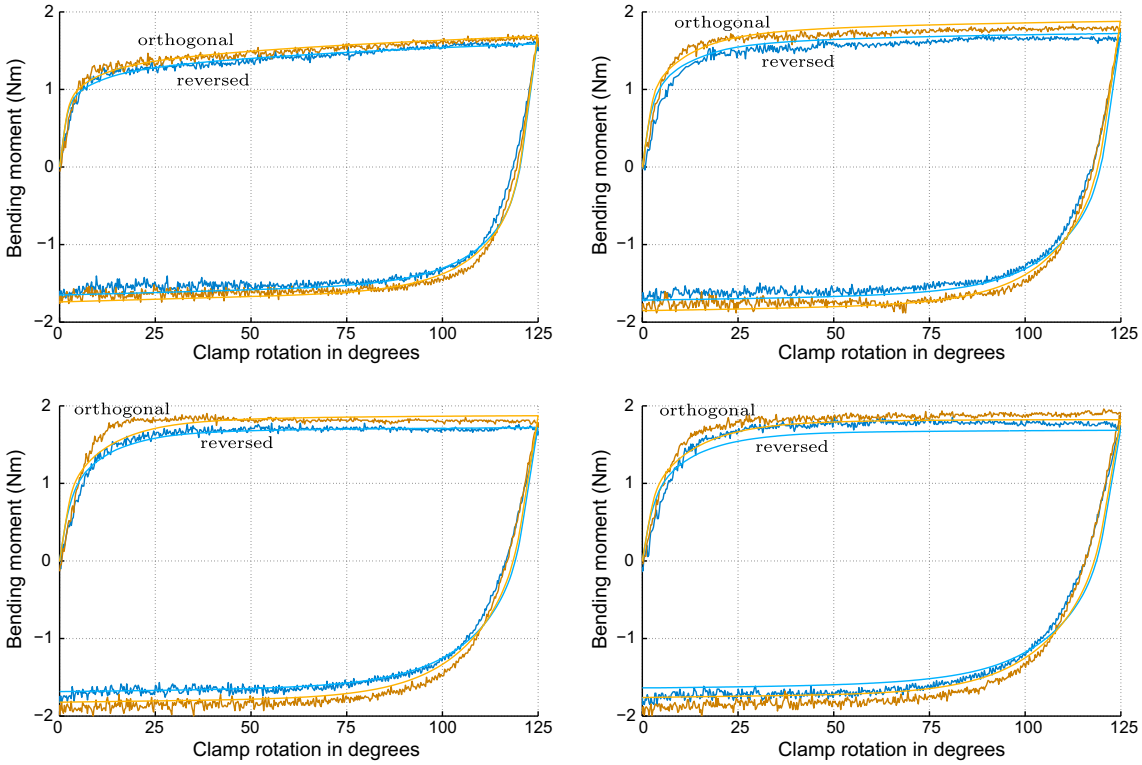

Fig. 18. Bending moments for the reversed and orthogonal bending tests, with a pre-deformation of 4.4% and 12.5% (top left and right) and 22.9% and 32.5% (bottom left and right).

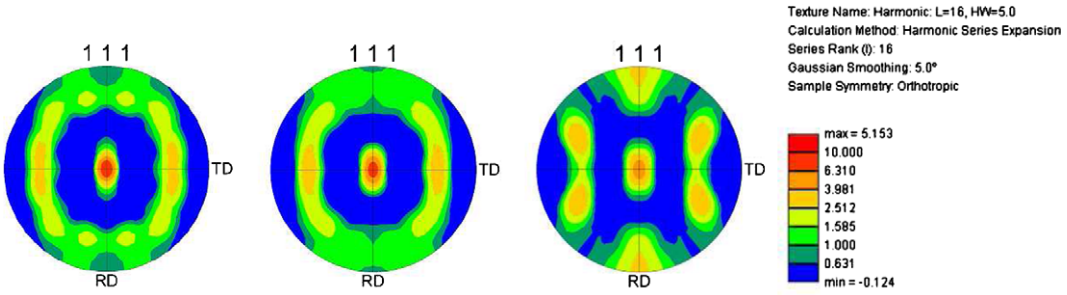

Fig. 19. From left to right, the OIM results for the as-received material, after 10% strain and after 35% strain during an uniaxial tensile test. Orthotropic symmetry is assumed and the high intensity in the as-received material indicates that the [1 1 1] axis of the crystals are perpendicular to the plane of the sample.

deformation. For the as-received material, a high concentration is found in the center of the pole-figure which indicates that the [1 1 1] axis of the b.c.c. crystal structure and its family of orientations is oriented along the normal of the sample surface ($\vec{e}_3$). This is also the case for the second sample, although a small change can be observed. For the third sample however, the [11 1] b.c.c. axes, and its family of orientations, have moved to different orientations. This is indicated by an number of spots with increased intensity along the circumference of the pole-figure, indicating a noticeable change in texture. The model used in this paper does not address the evolution of texture. Therefore it is not recommended to use this model for deformations larger than 35% strain.

The present version of the modified Teodosiu model does not predict extra hardening as a function of the reorientation of the crystals (Li et al., 2003b, 1997, 1998). Nevertheless, predictions for strains up to 30% during the monotonic loading experiments do provide satisfactory results.

6. Conclusions

- The plain strain pure bending experiment is a valuable experiment enabling large amplitude, repeated loading, reversed and orthogonal strain path changes, and a proper analysis of elastic springback effects.
- During the pure bending experiment, the strain distribution through the material thickness is non-homogeneous and provides a realistic complementary set of experimental data (representative for real forming processes). This is particularly relevant to enhance the description of kinematic hardening effects.
- The model of Wang et al. (2006, 2008) has been used, and the parameters for the DC06 material (Corus, the Netherlands) have been determined for a combination of different experiments: plain strain pure bending, uniaxial and plane-strain tension and a simple shear test.

- The values for s_{sat} and c_d are remarkably different from the values found in literature for the same material quality. It is believed that the values $s_{sat} = 128$ MPa and $c_d = 11$, are well describing the material hardening at large amplitude repeated loading, since the present results rely on a wider scope of experimental data.
- Additional through-thickness strain distribution measurements would be recommended for future research, although the measurements are not trivial. However, in the past, several measurements on our pure bending samples have shown that the sheet thickness of the specimens does not change, neither does the height of the samples (direction parallel to the rotational axis). Therefore a plain strain condition can be assumed which implies that the neutral line during the bending experiments is always in the center of the specimen. The resulting through-thickness strain distribution is therefore kinematically well controlled.
- The validation method combines the following aspects: (1) A well defined material deformation history, (2) A well defined experimental setup for the verification procedure without friction, contact or any other boundary effects, (3) A unique bending test, enabling a well controlled deformation state in the sample and (4) A sequence of forming steps which has not been used in the parameter identification method.
- During monotonic loading, where the strain distribution through the sample thickness is uniform and for strains larger than 0.3, the numerical prediction with the parameter set for the DC06 material underestimates the experimental findings.
- For strains larger than 30% during a uniaxial tensile test, the material texture has changed noticeably, which needs to be incorporated as well.
- An extra term, describing the texture dependent evolution of the hardening should be added to enhance the model.

Acknowledgements

The authors thank Till Clausmeyer from the Dortmund University of Technology for doing additional computational work during the revision phase of this paper.

References

Antonelli, L., Salvini, P., Vivio, F., Vullo, V., 2007. Identification of elasto-plastic characteristics by means of air-bending test. Journal of Materials Processing Technology 183, 127–139.

Boers, S.H.A., Geers, M.G.D., Kouznetsova, V.G., 2009. Contactless and frictionless pure bending. Experimental Mechanics, 1–11. ISSN 0014-4851.

Bouvier, S., Alves, J.L., Oliveira, M.C., Menezes, L.F., 2005. Modelling of anisotropic work-hardening behaviour of metallic materials subjected to strain-path changes. Computational Materials Science 32, 301–315.

Bouvier, S., Gardey, B., Haddadi, H., Teodosiu, C., 2006a. Characterization of the strain-induced plastic anisotropy of rolled sheets by using sequences of simple shear and uniaxial tensile tests. Journal of Materials Processing Technology 174, 115–126.

Bouvier, S., Haddadi, H., Levée, P., Teodosiu, C., 2006b. Simple shear tests: experimental techniques and characterization of the plastic anisotropy of rolled sheets at large strains. Journal of Materials Processing Technology 172, 96–103.

Bouvier, S., Teodosiu, C., Haddadi, H., Tabacaru, V., 2003. Anisotropic work-hardening behaviour of structural steels and aluminium alloys at large strains. Journal de Physique IV France 105, 215–222.

Carbonnière, J., Thuillier, S., Sabourin, F., Brunet, M., Manach, P.Y., 2009. Comparison of the work hardening of metallic sheets in bending-unbending and simple shear. International Journal of Mechanical Sciences 51, 122–130.

Christodoulou, N., Woo, O.T., MacEwen, S.R., 1986. Effects of stress reversal on the work hardening behavior of polycristalline copper. Acta Metallurgica 34, 1553.

Flores, P., Duchêne, L., Bouffioux, C., Lelotte, T., Henrard, C., Pernin, N., Van Bael, A., He, S., Duflou, J., Habraken, A.M., 2007. Model identification and fe simulations: effect of different yield loci and hardening laws in sheet forming. International Journal of Plasticity 23, 420–449.

Haddadi, H., Bouvier, S., Banu, M., Maier, C., Teodosiu, C., 2006. Towards an accurate description of the anisotropic behaviour of sheet metals under large plastic deformations: modelling, numerical analysis and identification. International Journal of Plasticity 22, 2226–2271.

Hasegawa, T., Yakou, T., 1975. Deformation behavior and dislocation structures upon stress reversal in polycrystalline aluminum. Materials Science and Engineering 20, 267.

Hiwatashi, Shunji, Bael, Albert van, Houtte, Paul van, Teodosiu, Cristian, 1997. Modelling of plastic anisotropy based on texture and dislocation structure. Computational Materials Science 9, 274–284 (Department MTM, Katholieke Universiteit Leuven, Leuven, Belgium, LPMTM-CNRS, Université Paris-Nord, Paris, France).

Hiwatashi, Shunji, Bael, Albert van, Houtte, Paul van, Teodosiu, Cristian, 1998. Prediction of forming limit strains under strain-path changes: applications of an anisotropic model based on texture and dislocation structure. International Journal of Plasticity 14, 647–669 (Department MTM, Katholieke Universiteit Leuven, Leuven, Belgium, LPMTM-CNRS, Université Paris-Nord, Paris, France).

Li, S., Hoferlin, E., Van Bael, A., Van Houtte, P., Teodosiu, C., 2003a. Finite element modeling of plastic anisotropy induced by texture and strain-path change. International Journal of Plasticity 19, 647–674.

Li, Saiyi, Hoferlin, Eric, Bael, Albert v., Houtte, Paul v., Teodosiu, Cristian, 2003b. Finite element modeling of plastic anisotropy induced by texture and strain-path change. International Journal of Plasticity 19, 647–674 (Department of Metallurgy and Materials Engineering, Katholieke Universiteit Leuven, Belgium).

Lou, X.Y., Li, M., Boger, R.K., Agnew, S.R., Wagoner, R.H., 2007. Hardening evolution of az31b mg sheet. International Journal of Plasticity 23, 44–86.

Nesterova, E.V., Bacroix, B., Teodosiu, C., 2001a. Experimental observation of microstructure evolution under strain-path changes in low-carbon if steel. Material Science and Engineering A309-310, 495–499.

Nesterova, E.V., Bacroix, B., Teodosiu, C., 2001b. Microstructure and texture evolution inder strain-path changes in low-carbon if steel. Metallurgical and Materials Transactions 32A, 2527–2538.

Omerspahic, E., Mattiasson, K., Enquist, B., 2006. Identification of material hardening parameters by three-point bending of metal sheets. International Journal of Mechanical Sciences 48, 1525–1532.

Peeters, B., Kalidindi, S.R., Teodosiu, C., Van Houtte, P., Aernoudt, E., 2002. A theoretical investigation of the influence of dislocation sheets on evolution of yield surfaces in single-phase b.b.b. polycrystals. Journal of the Mechanics and Physics of Solids 50, 783–807.

Peeters, B., Seefeldt, M., Kalidindi, S.R., Van Houtte, P., Aernoudt, E., 2001a. The incorporation of dislocation sheets into a model for plastic deformation of b.c.c. polycrystals and its influence on *r*-values. Materials Science and Engineering, 188–191.

Peeters, B., Seefeldt, M., Teodosiu, C., Kalidindi, S.R., Van Houtte, P., Aernoudt, E., 2001b. Work hardening/softening behaviour of b.c.c. polycrystals during changing strain paths: I an integrated model based on substructure and texture evolution, and its prediction of the stress-strain behaviour of an if steel during two-stage strain paths. Acta Materialia 49, 1607–1619.

Simo, J.C., Hughes, T.J.R., 1998. Computational Inelasticity. Springer Verlag.

Tan, Z., Persson, B., Magnusson, C., 1995. Plastic bending of anisotropic sheet metals. International Journal of Mechanical Sciences 37 (4), 405–421.

Teodosiu, C., Hu, Z., 1997. Microstructure in the continuum modelling of plastic anisotropy. In: Proceedings of the 19th Riso International Symposium on Materials Science: Modelling of Structure and Mechanics of Materials from Microscale to Product, pp. 149–168.

Teodosiu, C., Hu, Z., 1998a. Evolution of the intragranular microstructure at moderate and large strains: modelling and computational significance. Simulation of Materials Processing: Theory, Methods and Applications 82, 173–182 (Department of Mechanical Engineering, Korea advanced Institute of Science and Technology, South-Korea).

Teodosiu, C., Hu, Z., 1998b. Microstructure in the continuum modelling of plastic anisotropy. In: Proceedings of 19th Riso International Symposium on Material's Science: Modelling of Structure and Mechanics of Materials from Microscale to Product. Riso National Laboratory, Roskilde, Denmark, pp. 149–168.

Viatkina, E., 2005. Micromechanical modelling of strain path dependency in FCC metals. Ph.D. Thesis, Dept. of Mechanical Engineering, Eindhoven University of Technology, 2005. Dept. of Mechanical Engineering, TU/e.

Wang, J., Levkovitch, V., Reusch, F., Svendsen, B., 2006. Modeling and simulation of directional hardening in metals during non-proportional loading. Journal of Materials Processing Technology 177, 430–432.

Wang, J., Levkovitch, V., Reusch, F., Svendsen, B., Huetink, J., van Riel, M., 2008. On the modeling of hardening in metals during non-proportional loading. International Journal of Plasticity 24, 1039–1070.

Weinmann, K.J., Rosenberger, A.H., Sanchez, L.R., 1988. The bauschinger effect of sheet metal under cyclic reverse pure bending. Annals of the CIRP 37 (1), 289–293.

Yoshida, F., Urabe, M., Toropov, V.V., 1998. Identification of materials parameters in constitutive model for sheet metals from cyclic bending tests. International Journal of Mechanical Sciences 40 (2–3), 237–249.

Zhao, S.X., Kuang, Z.-B., 2006. An integral non-proportional cyclic plasticity model taking into account path dependencies. International Journal of Mechanical Sciences 48, 224–233.